3D PRINTING OF MICRONEEDLES VIA EMBEDDED 3D PRINTING USING AN ASSOCIATIVE SURFACTANT SYSTEM

A Thesis
IN
Mechanical Engineering

Presented to the Faculty of the University
of Missouri–Kansas City in partial fulfillment of
the requirements for the degree

MASTER OF SCIENCE

by
ROMARIO DYKE

B. Sc, University of Missouri-Kansas City, 2019

Kansas City, Missouri
2022

3D PRINTING OF MICRONEEDLES VIA EMBEDDED 3D PRINTING USING AN ASSOCIATIVE SURFACTANT SYSTEM

Romario Dyke, Candidate for the Master of Science Degree

University of Missouri–Kansas City, 2022

ABSTRACT

Microneedles are drug-delivery devices specially adapted to penetrate the outermost layer of the epidermis (stratum corneum). These devices have gained popularity over the last decades because they provide non-invasive drug delivery options. There are many types of microneedles to suit a wide variety of applications. This work is focused on using new lipid-hydrogel materials to fabricate microneedles using a liquid-in-liquid 3D printing process combining embedding and associative liquid-in-liquid 3D printing approaches. Although liquid-in-liquid 3D printing was successfully applied in previous research, printing at the microscale introduces additional complexities. To successfully fabricate microneedles at the microscale with good shape fidelity and appropriate mechanical properties, it is crucial to study the print parameters (printing process), the material properties, and how they work together. Through experiments, we investigated the effects of various print parameters, print materials, and suspension baths on the quality of the

3D-printed microneedles.

APPROVAL PAGE

The faculty listed below, appointed by the Dean of the School of Computing and Engineering, have examined a thesis titled "3D Printing of Microneedles via Embedded 3D Printing using an Associative Surfactant Sytstem," presented by Romario Dyke, candidate for the Master of Science degree, and hereby certify that in their opinion it is worthy of acceptance.

Supervisory Committee

Zahra Niroobakhsh, Ph.D., Committee Chair
Division of Energy, Matter, and Systems
UMKC School of Science and Engineering

Antonis P Stylianou, Ph.D.
Division of Energy, Matter, and Systems
UMKC School of Science and Engineering

Karl Kador, Ph.D.
Department(s) of Biomedical Sciences, Ophthalmology
UMKC School Of Medicine

CONTENTS

ILLUSTRATIONS

TABLES

ACKNOWLEDGEMENTS

I thank Dr. Zahra Niroobakhsh, for her time and invaluable insight. Special thanks to Ph.D. students Houman Honaryar and Saba Amirfattahi for helping me with material preparation, testing, and thesis proofreading. The help of Dr. Kun Cheng, from the UMKC School of Pharmacy, with the ordering of peptides is appreciated. I am also grateful to Dr. Donggao Zhao and Electron Microscope Laboratory of the UMKC School of Dentistry for the help with SEM measurements. I also want to thank Collin Hurshman, the former undergraduate research assistant in our research group, for his contribution to the g-code design. I acknowledge that without your help, this work would not be possible. I am thankful to the members of my thesis committee, Dr. Antonis P Stylianou and Dr. Karl Kador for their valuable insight and for serving as committee members. Thank you all. This work is supported by UMKC Funding for Faculty Excellence Award (FFE-2021) and ACS-PRF grant (PRF #61716-DNI9) partially.

CHAPTER 1

INTRODUCTION

Drug delivery systems regulate the distribution of drugs into and throughout the body [5]. These systems play an essential role in successfully administering medications in biological systems. While there are many forms of drug delivery administration systems, oral and intravenous administrations are the most common. However, these systems are not always effective for delivering all active drugs [6, 7]. Despite their convenient administration and cost-effectiveness, oral administration, such as pills and liquid medicine, has limitations. The most notable being the first-pass metabolism. First-pass metabolism describes drug concentration degradation before reaching the target site [7–11]. Intravenous administration, using hypodermic needles, significantly improves the bioavailability of drugs and eliminates the risk of first-pass metabolism during oral administration [11, 12]. Although the drug concentration and effectiveness are enhanced with hypodermic needles, they are associated with pain, and low patient compliance [7–9, 11]. Therefore, there has been a surge in research on microneedle technologies to ease the patient burden.

1.1 Microneedles

Microneedles are microscale protrusions designed to transport drugs across the skin stratum corneum, the epidermis outermost layer, and into the body [5, 13, 14]. Microneedle systems have become increasingly popular in the pharmaceutical and medical device industries because they are minimally invasive and provide a painless option for drug delivery [11, 15]. In addition, they are relatively easy to use, which allows patients to administer the medication themselves, eliminating the need for medical personnel [16]. This technology is especially advantageous for frequently used drugs, such as insulin, taken daily by people with diabetes to regulate blood sugar [16].

Microneedle usage for various medical applications has been around for many years. Yet, it was in the mid-1990s that researchers started to evaluate how to manufacture microneedles for drug delivery [1, 17]. Initially, solid microneedles were used for the patient's pre-treatment to enhance skin permeability before administering drugs. In those cases, hollow microneedles were used for skin infusion [17]. Other types of microneedles include solid, coated, dissolving (as shown in Figure 1), porous, swellable hydrogels, and merged tips, [1, 18].

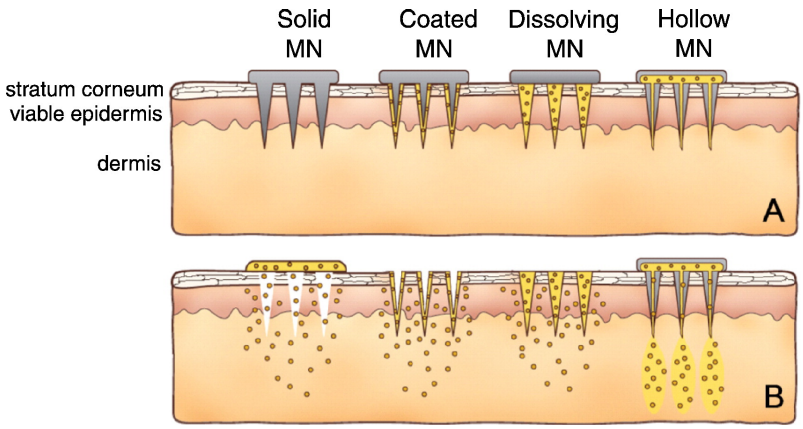

Figure 1: Methods of drug delivery to the skin using microneedles. Reprinted from [1], Copyright (2012), with permission from Elsevier.

Today, microneedles are used in numerous drug delivery applications expanding innumerable administration routes, including transdermal, ocular, and intracellular [17]. The applications dictate the design of the microneedle. Different applications will call for microneedles with various geometrical factors such as tip radius, height, and base diameter. Microneedle array density, spacing, and materials are other factors that the application dictates and need to be considered during the design phase. Microneedles that can effectively penetrate the skin are critical in drug delivery applications. Understanding the relationship between microneedle application, design, and manufacturing parameters will provide insight into producing functional microneedles [18].

This research focuses on using a new material, i.e., lipid-hydrogel, to fabricate microneedles from an associative surfactant system. The embedded 3D printing via pneumatic extrusion limited the microneedle geometry to cylinders and cones. We will first

understand how to manufacture microneedles with good mechanical properties before attaining effective penetration using embedded 3D printing.

1.2 Manufacturing of Microneedles

Historically, microneedles have been manufactured using micro-molding techniques or micro-injection molding. Micro-injection molding is a specialized manufacturing method that produces miniature components requiring precision with micron tolerances (10 to 100 μm) [1, 19, 20]. Other conventional manufacturing methods include, but are not limited to, direct laser micromachining, chemical wet etching, electrical discharge machining, UV-lithography, and deep reactive-ion etching [18]. On the other hand, 3D printing technology has revolutionized the medical device industry, and its influence can now be seen in the 3D printing of microneedles [17]. 3D printing technologies that have been employed for microneedle fabrication include the fused deposition modeling (FDM) method, stereolithography (SLA), digital light processing (DLP), and two-photon polymerization (2PP) [21, 22]. This work uses an embedded 3D printing approach to fabricate microneedles.

1.3 Liquid-in-liquid 3D Printing

Liquid-in-liquid 3D printing is a technique where a liquid, referred to as the printing material or ink, is extruded into another fluid that acts as a liquid or gel bath phase [23]. The support bath prevents the extruded structure from collapsing during and after extrusion. The liquid-in-liquid 3D printing techniques can be divided into two main

subsets; embedded 3D printing, also known as the freeform reversible embedding of suspended hydrogels (FRESH) printing, [24, 25] and associative liquid-in-liquid 3D printing [26]. In the embedded printing platforms, the favorable rheological properties of the bath phase enable the printing [24, 25]. In contrast, in the associative approach, the interaction/association between the two phases (bath and printing materials) can stabilize the printed materials [26,27]. Our research group pioneered the use o surfactant self-assembly in associative liquid-in-liquid 3D printing, where relatively complex structures with tunable mechanical properties and internal nanostructural ordering were 3D printed from an aqueous solution of surfactants [23,26,28]. Embedded 3D printing, on the other hand, has been studied extensively for various material systems [24, 25]. In these techniques, the rheological properties of the print material and support bath are of equal significance. The success of the process depends on whether these properties are appropriately tuned. When properly formulated, the support bath has shear-thinning and self-healing properties that allow for liquid-in-liquid 3D printing [29]. When the print material is extruded into the support bath, the support bath yields and fluidizes at the location of the moving nozzle. As a result, the nozzle applies stress; upon removing this stress, the bath resolidifies and keeps the extruded material in place until photopolymerization is completed [23].

1.4 Task Description

In this project, we use an associative surfactant system composed of biological surfactants (lipids), water, and lipid oil (castor oil) to print microneedles through the liquid-in-liquid 3D printing process. Previous studies have demonstrated that associative

surfactant systems (such as surfactant-water-oleic acid oil) can be used to fabricate complex structures with mechanically tunable and internal nanostructured phases [23, 30, 31]. The experimental and simulation studies on this system suggested that forming nanostructures with various morphologies (e.g., lamellar or hexagonal) at the liquid-liquid interface is the enabling factor for printing [28,31–33]. This associative liquid-in-liquid 3D printing technique allows using a relatively low viscous aqueous solution containing surfactants (such as lipids in this work) and prepolymer to print complex microneedle structures in an appropriately chosen lipid oil bath.

In this study, we will use a new associative material system (i.e., lipid, oil, water) following the same liquid-in-liquid 3D printing approach as used in previous studies [23, 30, 31]. However, to be able to print complex microstructures such as microneedles, we will incorporate nanoparticles (i.e., fumed silica) into the primary liquid oil bath to create a gel-like support bath similar to the embedded 3D printing approach discussed in the previous section. Thus, we combine associative liquid-in-liquid 3D printing and embedded 3D printing approaches for this project. In addition, the printability of different lipid compositions is analyzed to understand how they react in different environments when subjected to other print parameters.

The overarching aim of this research is to explore the appropriate lipid-hydrogel composition, investigate printing parameters, tune the rheological properties of the support bath, and evaluate the printed microneedle structure and mechanical properties. For the **first objective**, we will study four lipids and prepolymer

combinations and two gel baths. For the **second objective**, we will explore various printing parameters, such as print pressure, print speed, print nozzle diameter, and rheological properties of the support bath. The factors are numerous and interrelated; this study should create a framework to quantify and optimize print parameters. As the **third objective**, we need to ensure microneedles have good mechanical properties and can penetrate the mimic skin. Therefore, microneedles with good mechanical properties and penetration capability should be at the center of functional design. To evaluate the mechanical properties, compression tests will be conducted. From the compression tests, force-displacement and stress-strain curves data will be obtained and analyzed to find fracture force and compressive modulus for each lipid composition.

CHAPTER 2

MATERIALS AND METHODS

2.1 Preparation of Printing Liquid

Each aqueous solution used as the printing liquid is comprised of lipids (as the surfactant), a prepolymer mixture, and a photoinitiator (Figure 2). As explained in section 1.4, biological surfactants (lipids) are used for this study, as they make up the majority of cells and tissues [34]. The lipid used is L-α-phosphatidylcholine (95%) (also known as soy PC or soy lecithin), purchased from Avanti Polar Lipids, Inc. Soy PC is mixed with deionized water and the appropriate solvent for lipids. Reagent alcohol (ethanol, Ricca Chemical) is used as the solvent for soy PC that consists of 90.48 wt% ethyl alcohol, 5 wt% isopropyl alcohol, and 4.52 wt% methyl alcohol. Prepolymer mixtures are composed of polyethylene glycol diacrylate (PEGDA, M_n = 700 gr/mol), 1-hydroxycyclohexyl phenyl ketone (HCPK, as the photoinitiator). A macromolecule drug model is added for some of the compositions, a peptide amphiphile (PA) which consists of a sequence of 16 hydrocarbon chains attached to 3 Valine, 3 Alanine, and 3 Lysine amino acids (C16V3A3K3) [35] synthesized by GenScript. Four aqueous printing solutions are made by combining the components mentioned earlier and are referred to as soy PC 1, soy PC 2, soy PC 3, and soy PC 4 (see the detailed description in Table 1).

Table 1: Compositions summary of the aqueous solutions used as printing

Composition	**soy PC 1**	**soy PC 2**	**soy PC 3**	**soy PC 4**
PEGDA (ml)	3.6	3.6	5.4	8.5
HCPK (gr)	0.2016	0.2016	0.3024	0.476
PA (gr)	0.1035	0.111	-	-
soy PC (ml)	6.4	6.4	4.6	1.5
soy PC in solvent: soy PC conc. (wt%)	21.66	22.5	31.3	31.3
solvent: Ethanol(%):Water(%)	(76Eth:24W)	(76Eth:24W)	(76Eth:24W)	(76Eth:24W)

Notes*: Abbreviations are as follows; PEGDA: Polyethylene glycol diacrylate, HCPK: Hydroxycyclohexyl phenyl ketone, PA: Peptide amphiphile, W: water, Eth: ethanol, conc.: total stock concentration in solvent and soy PC: L-α-phosphatidylcholine*

2.2 Preparation of Support Bath

Castor oil (CO, Alfa Aesar), a lipid oil, is used as the primary component of liquid baths. Castor oil is mixed with nanoparticles to create a gel support bath to print microneedle structures (Figure 2). The fumed silica nanoparticles (NPs, (hydrophobic pyrogenic silica, HDK H30) have a primary particle size distribution of 12 nm and were generously provided by Wacker Chemie AG. In an effort to determine the most suitable support baths, different bath compositions are assessed. Castor oil baths with 5 and 6 wt.% nanoparticles are found to work best for this application, which will be explained in the results. To prepare the bath with 5 wt.% NP, 15 ml of castor oil is mixed with 0.75 gr of nanoparticles. Likewise, to prepare the 6 wt.% NPs bath, 15 ml of castor oil is mixed with 0.9 gr of NPs. The mixtures are manually stirred using a spatula until a homogeneous gel is obtained. To ensure that the mixture is uniform and void of air bubbles, it is placed

in a vacuum desiccator (SP Bel-Art) until air bubbles are no longer visible.

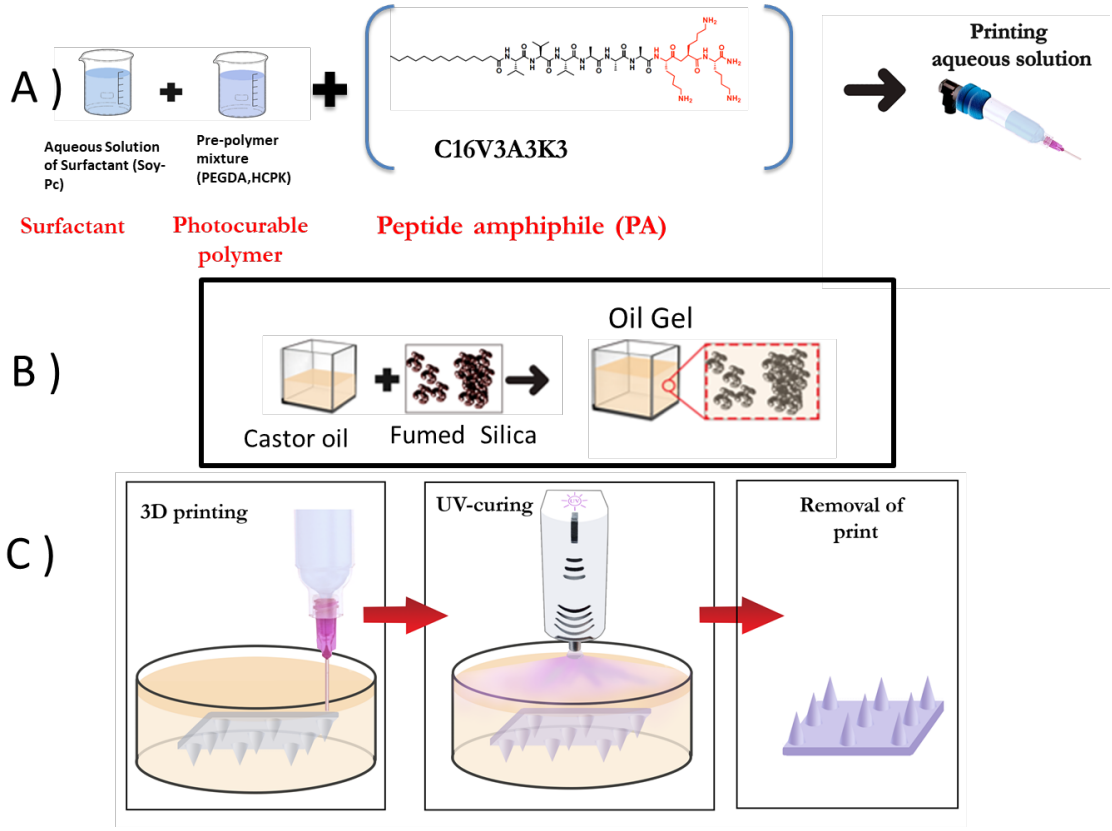

Figure 2: Schematic illustration of the printing process. (A) Preparation of printing solution, (B) preparation of gel bath, and (C) microneedle printing process.

2.3 Printing Procedure

Microneedle arrays are printed using a commercial bioprinter (CELLINK BIO X6) shown in Figure 3. A pneumatic configuration is utilized for dispensing print material. Printing material is loaded into the UV-shielding cartridge (volume of 3 ml) with a print nozzle (27 G and 30 G) attached. The cartridge is used as a reservoir from which the print material is extruded. The printer has six (6) pneumatic print heads where cartridges

are inserted and connected to air hoses via a cartridge adapter. In this experiment, only one print head is used.

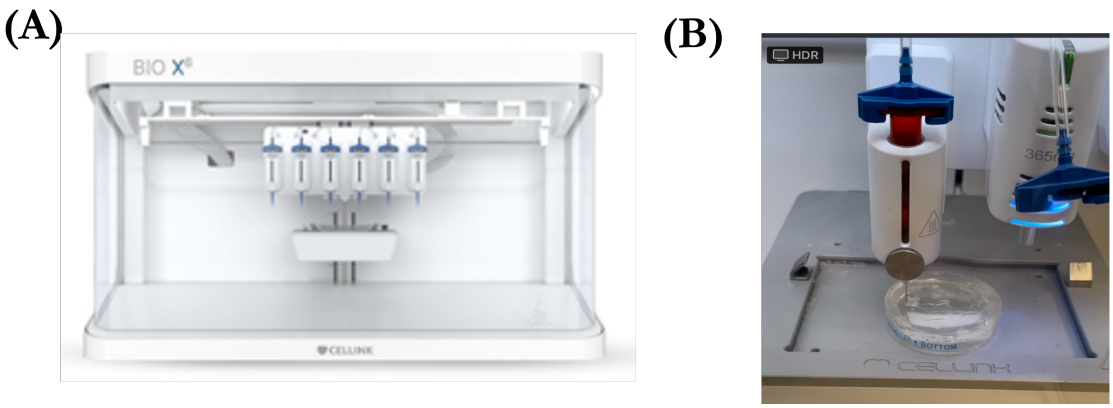

Figure 3: Cellink BIO X6 Bioprinter with pnuematic setup. (A) Cellink's Bio X6 printer [2]. (B) Cellink's Bio X6 setup for pneumatic extrusion with the UV-shielding cartridge (volume of 3 ml) and print nozzle loaded and inserted into a single printhead set up to print in a suspension bath.

G-code, a computer numerical control programming language with the path direction to create microneedles, is written in a notepad and uploaded to the printer interface. The G-code has commands to control extrusion and air pressure. This code commands the pneumatic print head when and where to move along the X and Y axis and how fast to move. There are also commands to tell the print bed how to move along the Z axis. The loaded cartridge contains a plastic piston located between the print material and the inlet air (at the outlet of the air hose). When the G-code commands extrusion, air pressure is applied, resulting in the dispensing of print material. The print material is dispensed while the pneumatic print head follows the tool path generated from the G-code. Two g-code variations are tested for printing; the first variation had microneedles printed upright, as

depicted in Figure 4, and the second variation had microneedles printed upside-down, as depicted in Figure 5. The second variation, printed upside-down microneedles, produced better shape fidelity. Microneedles that are printed upright did not have well-defined tips. The tip is the junction of the microneedle and print nozzle; the point of separation between the two could be the reason for creating defects on the microneedle tip.

Figure 4: Model Design 1. (A) shows path generated by G-code for right side up microneedle printing. (B) shows microneedle printed following path generated by G-code for right side up microneedle.

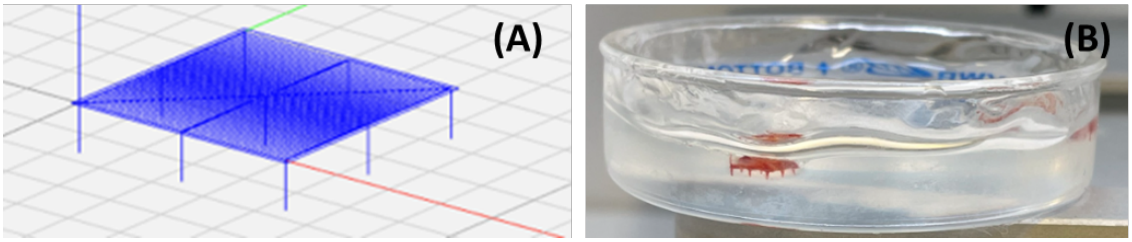

Figure 5: Model Design 2. (A) shows the path generated by G-code for upside-down microneedle printing. (B) shows microneedle printed following path generated by G-code for up-side down microneedle.

The print material is dispensed in the support bath, taking the form of a microneedle array. The microneedle array consists of two parts; a square substrate and microneedles (Figure 6). The G-code generates path instructions for a 5 $\times$ 5 mm substrate and

1.5 mm tall microneedles with 2.5 mm spacing between each microneedle. A 7 $\times$ 7 mm substrate design is implemented later on to better accommodate microneedles on the array. It is important to note the length of microneedles is not confined to the predetermined length of the G-code path. The print material, suspension bath, and print parameters all influence the resulting prints. After printing is completed, the microneedle is solidified through UV-curing. UV curing is conducted using a UV curing copper board made up of four (4) UV LEDs (365 nm, LED Engin) and four Copper heatsinks (13.2 mm $\times$ 12.1 mm, DFRobot). The UV module is powered by a DC power supply (Eventek) [23], a voltage of 3.5 V, and a current of 350 mA are used for curing [23]. The microneedle is extracted from the bath using a spatula. The gel-like nature of the support bath leaves gel residues on the microneedles. To remove the gels, the microneedle is submerged in Reagent alcohol (ethanol, Ricca Chemical). The duration of this washing process varied from 5 to 7 hours based on the concentration of nanoparticles in the support bath. Figure 2 illustrates the composition of the printing materials and support bath and a schematic picture of the microneedle printing process.

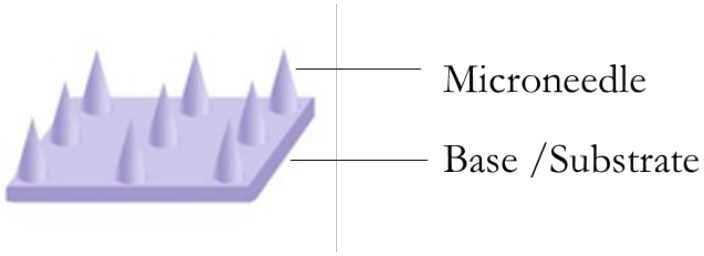

Figure 6: Schematic of the microneedle array.

2.4 Visualization

For visualization of microneedles, a table-stand digital microscope (Amscope, UTP200X003MP) with 10X-200X magnification and a built-in LED light source is used, as shown in Figure 7. Furthermore, a field-emission environmental scanning electron microscope (Philips XL30) has been used for visualizing nano- to micro-scale features of the microneedles.

Figure 7: Amscope digital microscope [3].

2.5 Mechanical Properties Characterization

The mechanical properties of the microneedles are assessed using a TA Instruments Discovery Hybrid Rheometer (DHR-3). The rheometer is operated in compression mode, and the parallel plate geometry with a diameter of 40 mm is used. The microneedle patch is directly removed from ethanol and placed on the bottom plate, and the top plate is lowered at 5 μm/s. Upon contact with the needles, the force measured by the top plate

and the displacement is recorded to obtain force-displacement curves and the failure force of the microneedles.

The mechanical properties of the printed material are assessed using the same method. For each material, samples are printed in square shapes (Figure 24). Samples are directly removed from ethanol and placed on the bottom plate, and the top plate is lowered at 5 μm/s. Upon contact with the sample, force and displacement are measured to produce force-displacement curves. Stress and strain data is obtained from the force-displacement information. The strain is the displacement divided by the initial distance between the top and bottom plates. The stress data is obtained by dividing the recorded force by the area of the samples; the area is calculated by multiplying the sides of printed samples (post-processing). Figure 8 shows a schematic illustration of the compression test setup.

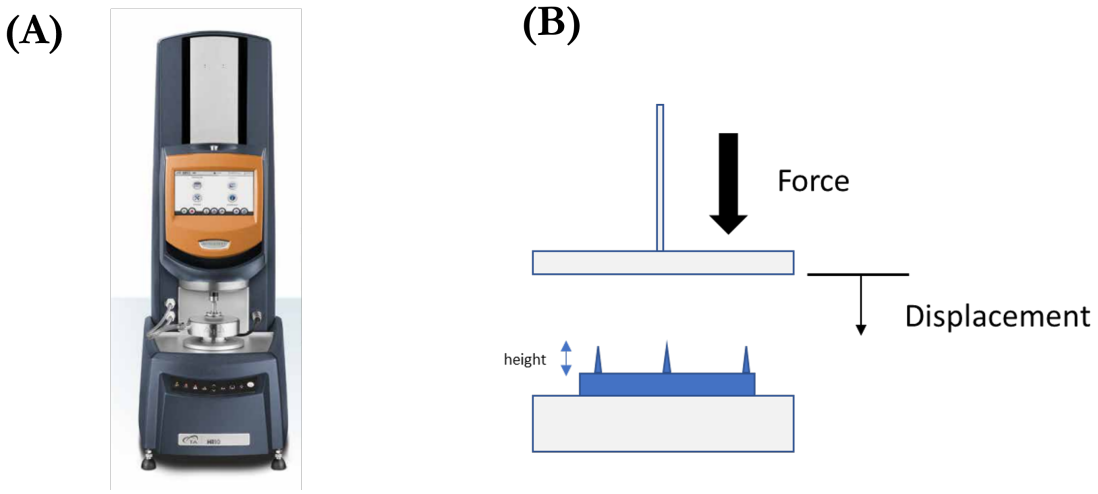

Figure 8: Compression test setup. (A) TA Instruments Discovery Hybrid Rheometer (DHR-3) [4]. (B) schematic of compression test conducted using TA Instruments Discovery Hybrid Rheometer (DHR-3).

2.6 Penetration Test Setup

To evaluate the ability of the microneedle to penetrate the skin, a polymeric film (Parafilm M, a blend of hydrocarbon wax, and a polyolefin, 127μm in thickness) is used. Parafilm is shown to be a suitable skin simulant in previous studies [36]. Each layer of wax is penetrated by manually pressing the microneedles until penetration or failure is observed.

CHAPTER 3

MICRONEEDLE PRINTING

3.1 Printing Parameters

The printer used in this work offers the option of tuning print pressure and print speed. To better understand the factors that affect printability, a relatively wide variety of print pressures, print material (See Table 1, and Figure 9), print speed, nozzle size, and support baths are tested. These factors are all interrelated, and some of them are related according to the Hagen-Poiseuille equation as demonstrated in Equation 3.1, where Q is flow rate, P pressure, d nozzle diameter, μ viscosity of printing liquid, and l is nozzle length [37–39]. Next, systematic analysis is used to identify the best print parameter combinations. From there, the objective is to optimize microneedles with the best mechanical behavior (hence, acceptable penetration) and printing quality.

$$Q = \frac{\pi P d^4}{128 \mu l}, \tag{3.1}$$

Based on Equation 3.1, increasing the print pressure and/or nozzle diameter will result in an increased flow rate. Print pressure and nozzle diameter demonstrate a directly proportional relationship to flow rate. Increasing the nozzle length and print material viscosity will result in a decreased flow rate because nozzle length and viscosity demonstrate an inversely proportional relationship to flow rate.

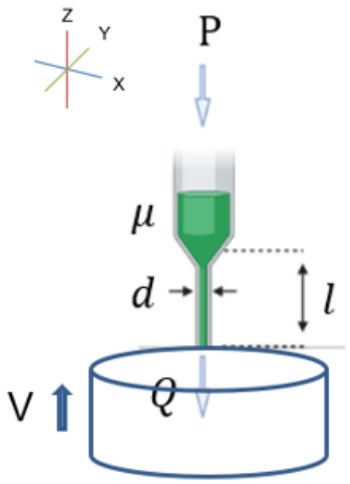

Figure 9: Schematic of print parameters where Q is flow rate, P pressure, d nozzle diameter, μ viscosity, l is nozzle length and V is print speed.

The printing speed, V, describes the speed at which the print head translates along the x, y, and z axes during printing. To print the microneedles, the nozzle moves along the z-axis while extruding. The print speed affects the volume of material that is extruded per unit time. To quantify the effects of the aforementioned parameters, microneedles are printed and analyzed.

3.1.1 Effect of Varying Printing Speed and Extrusion Pressure

Figure 10 shows a 3×3 microneedle array. Castor oil baths containing 6 wt.% NPs are used as the support medium for printing. Microneedle arrays are printed with soy PC 1. Six (6) print pressures, ranging from 40 kPa to 75 kPa, are used to determine the effects of print pressure on microneedle structure. Print speed for microneedles and base

(substrate) (300 mm/min), base print pressure (20 kPa), and nozzle size (30G) remained constant throughout this test. This combination of parameters produces longer and thicker microneedles when print pressure is increased, as depicted in Figure 10. As pressure affects the volumetric flow rate, the volume of extruded material is expected to increase by increasing pressure, resulting in longer and thicker microneedles.

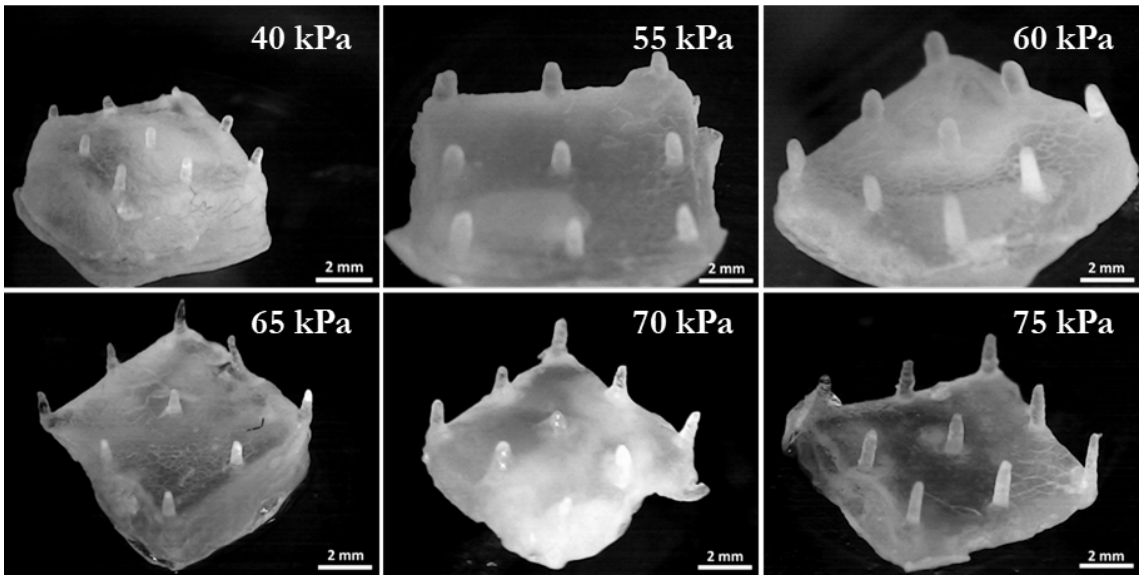

Figure 10: Microneedle arrays made by soy PC 1 printed in castor oil bath containing 6% NPs printed at varying microneedle extrusion pressure. The base extrusion pressure (20 kPa), print speed for microneedles and base (300 mm/min), and nozzle size (30G) are remained fixed.

Additional experiments are conducted using soy PC 2. In this test, a higher microneedle print speed is used (1200 mm/min). The base print speed (300 mm/min), base print pressure (20 kPa), and nozzle size (30G) remained constant. Microneedle print pressures varied between 10 kPa and 75 kPa. Figure 11 shows the 3×3 microneedle array printed using the aforementioned parameters.

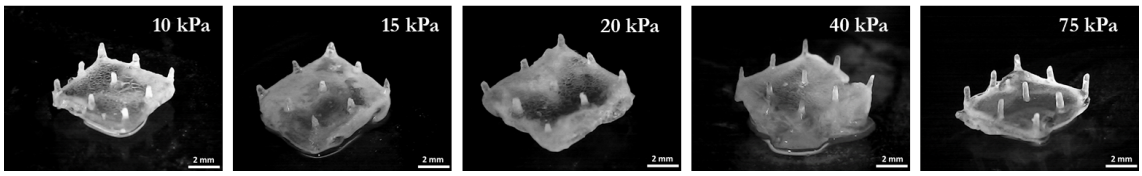

Figure 11: Microneedle arrays made by soy PC 2 printed in castor oil bath containing 6% NPs printed at varying microneedle extrusion pressure. The base extrusion pressure (20 kPa), print speed for microneedles and base (1200 mm/min), and nozzle size (30G) are remained fixed.

The microneedle length and thickness increased when microneedle print pressure is increased, as depicted in Figure 11, consistent with the results observed for the previous case (Figure 10), even though a higher microneedle print speed and different print material are used. This is because a higher volume of print material is extruded at higher pressures, resulting in longer, thicker needles.

Print pressure and speed are tested in parallel to examine the combination of print parameters on microneedle structures. Microneedle arrays are printed using print pressures of 10 kPa and 15 kPa at print speeds of 600 mm/min, 900 mm/min, and 1200 mm/min. Microneedle base print speed (300mm/min), microneedle base print pressure (20 kPa), and nozzle size (30G) are kept constant.

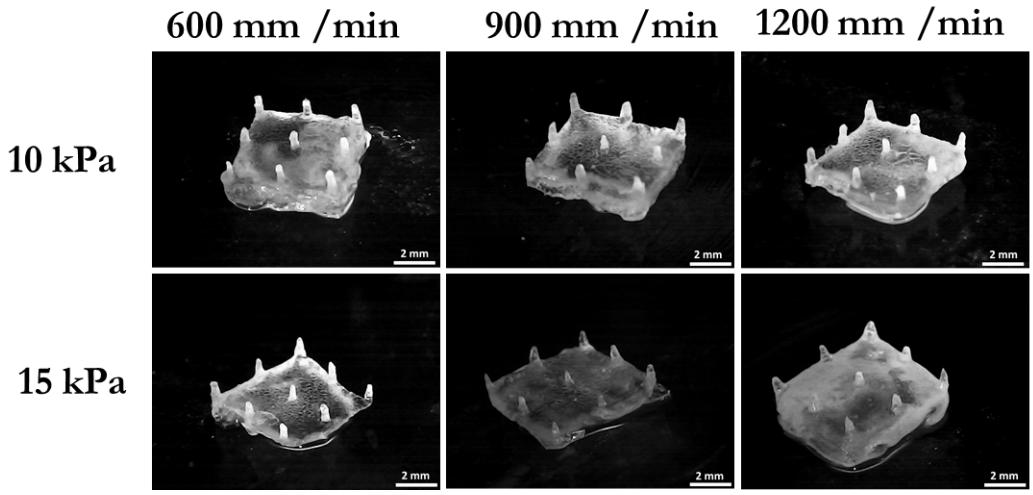

Figure 12: Microneedle arrays made by soy PC 2 printed in castor oil bath containing 6% NPs printed at varying microneedle extrusion pressure and print speed. Microneedle base print speed (300mm/min), microneedle base print pressure (20 kPa), and nozzle size (30G) are kept constant. Row 1: Microneedles printed at constant print pressure (10kpa) with increasing print speed (600mm/min - 1200mm/min). Row 2: Microneedles printed at constant print pressure (15kpa) with increasing print speed (600mm/min - 1200mm/min).

As shown in Figure 12, microneedles decreased in length with increasing the print speed at constant print pressure. This is because less print material volume is deposited per unit of time, resulting in shorter, more conical microneedles. However, increasing print pressure from 10 kPa to 15 kPa across each print speed did not yield significant changes in microneedle length. This can be attributed to the relatively small increase in pressure.

3.1.2 Effect of Varying Printing Nozzle Size

In addition to the print pressure and speed, the nozzle size is an equally-important print parameter. Larger diameter nozzles will produce thicker microneedles, provided that the print speed and print pressure are the same; more print material will be extruded with larger diameter nozzles.

In an attempt to verify this claim, a print nozzle of 27 G with a larger internal diameter of 0.2 mm compared to a 30 G nozzle (with an inner diameter of 0.15 mm) is used to print microneedle arrays. As it is evident in Figure 13, these microneedles printed with 27 G nozzle are, in general, thicker and longer than microneedles printed with a 30 G nozzle since nozzle size is directly proportional to the flow rate.

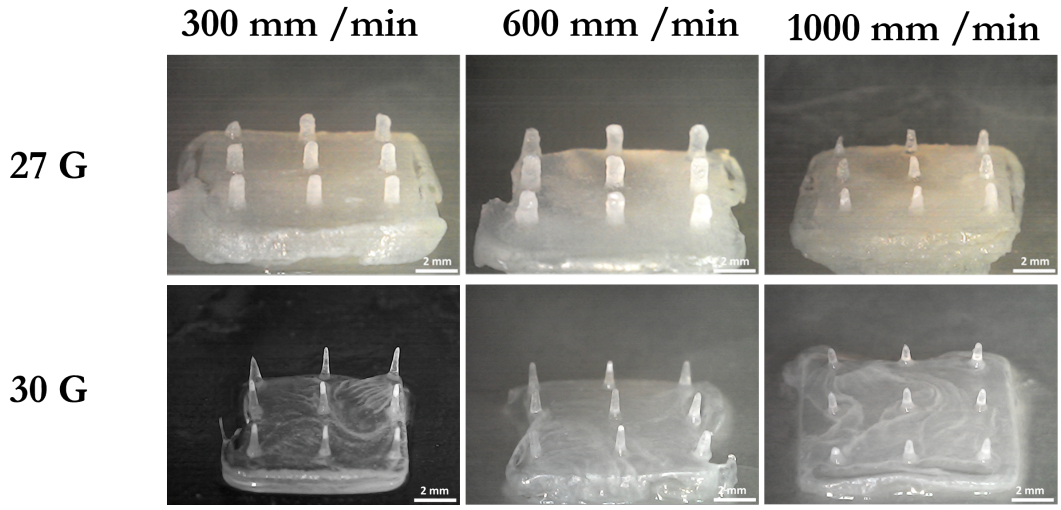

Figure 13: Microneedle arrays made by soy PC 4 printed in castor oil bath containing 5% NPs printed using a 27 G and 30 G nozzle. The microneedle base and microneedles are printed using an extrusion pressure of 20 kPa.

The 30 G nozzle produced better microneedles for skin penetration applications

due to its smaller thickness, more printing fidelity, and more conical shape. Even though the 27G nozzle microneedles are thicker, their cylindrical shape makes them disadvantageous for skin penetration. To continue optimizing for skin penetration, additional prints are created with soy PC 3 using 30 G nozzles.

3.1.3 Substrate Size

Figure 14 shows 3×3 microneedle array structures. The size of the base of the microneedle is increased from 5×5 mm^2 to 7×7 mm^2 to accommodate the microneedles along the edges better. The print pressures are set to 20 kPa and 50 kPa. Print speed (600 mm/min), base print pressure (20 kPa), and nozzle size (30G) are kept constant. The printed microneedles at a higher pressure of 50 kPa are longer and thicker when compared to the microneedles printed using 20 kPa, consistent with previous tests, provided other factors remained constant.

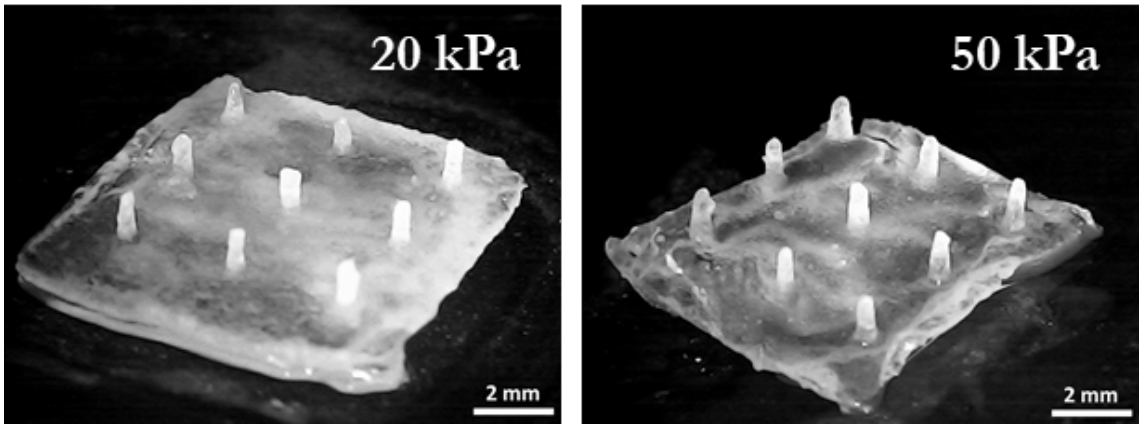

Figure 14: Soy PC 3 microneedle arrays printed in the castor oil bath containing six (6) wt.% NPs using 30 G nozzle. For these prints, print speed is kept constant at 600 mm/min, and print pressure is varied to investigate the effects of print pressure on the microneedle characteristics.

3.1.4 Effect of Varying Nanoparticles Concentrations in the Bath

UP to this point, all the microneedles are printed in a bath containing 6 wt.% NP. After printing, washing, and removing residual gels for the microneedles from the 6 wt.% NPs bath proved time-consuming and added complexity to the process. In an effort to make removal easier and less time-consuming, castor oil baths with 5 wt.% NPs is used after this test. Microneedles are printed using a 25 kPa print pressure to check this new suspension bath composition. This print pressure is an arbitrary value, chosen solely for suspension bath testing, not to test the effects of pressure.

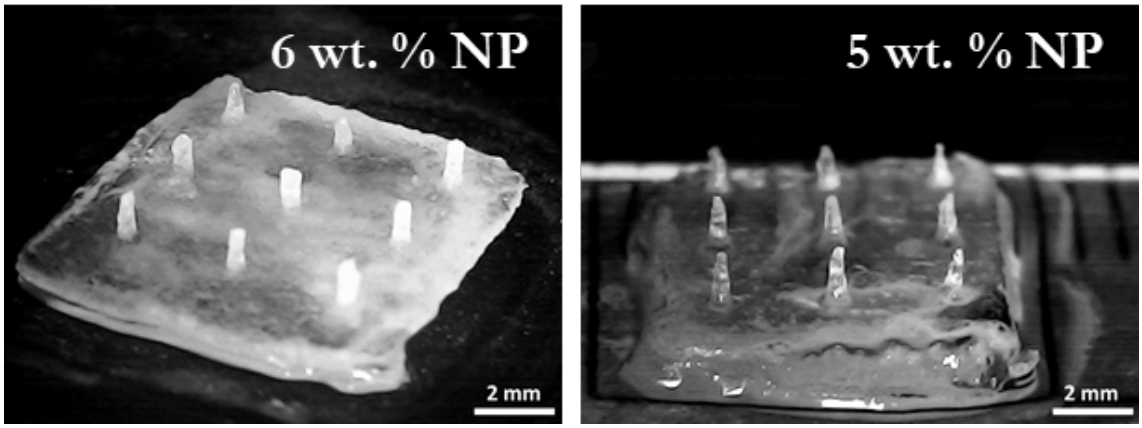

Figure 15: Soy PC 3 microneedle arrays printed in the castor oil bath containing 6 wt.% and 5 wt.% NPs using 30G nozzle. For these prints, print speed is kept constant at 600 mm/min, and print pressure is 20 kPa (6 wt.% NP) bath and 25 kPa (5 wt.% NP).

Implementing the 5 wt.% NPs bath resulted in easier microneedles removal and an unexpected shape change. This difference in shape can be observed in Figure 15. Compared to the microneedles printed in 6 wt.% NPs bath, the microneedles printed in the 5 wt.% NPs bath interestingly appears to be more conical. The different viscoelastic gel-like properties of each bath are likely responsible for the change in the print material behavior.

The results obtained using the 5 wt.% NPs baths are favorable, as conical microneedles are better suited for skin penetration. Subsequently, the next set of prints is supported by this bath to see if the results would be similar. In addition, various combinations of print parameters are used to determine any improvement in the microneedle characteristics. Figure 16 below shows microneedles printed using soy PC 4. Three print speeds and pressures are used for these prints while maintaining a constant base print

pressure (20 kPa) and nozzle size (30G).

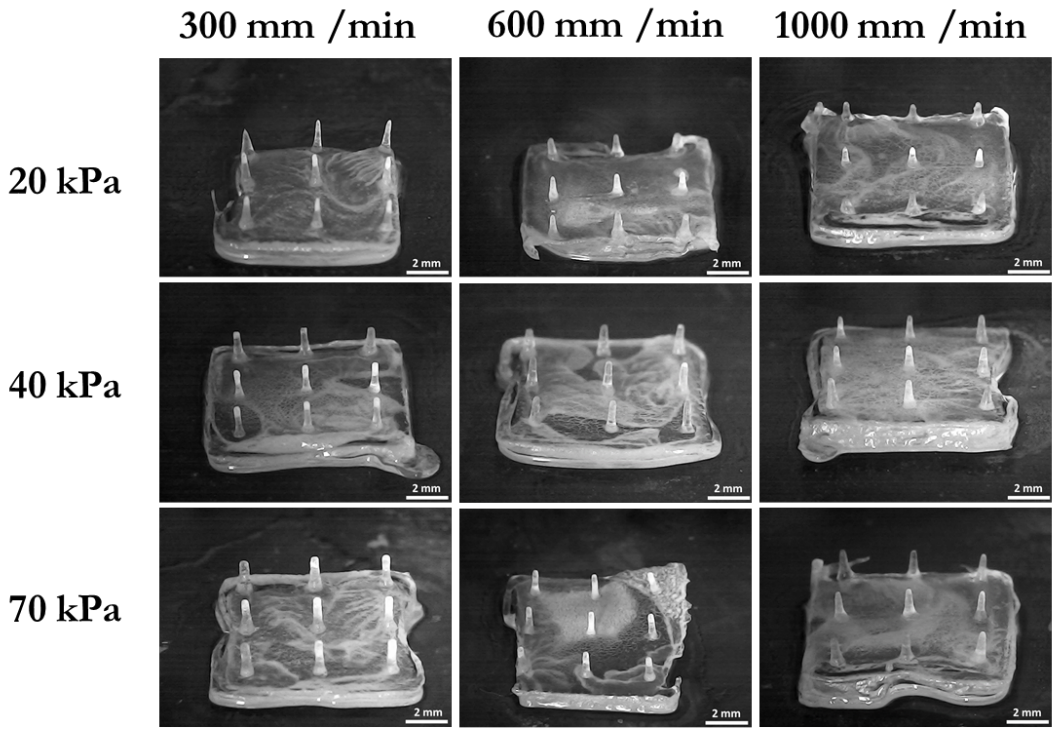

Figure 16: Soy PC 4 microneedle structures printed in castor oil baths containing 5 wt.% NPs using 30G nozzle. For these prints, print pressure and print speed varied to show the effects of both parameters.

As depicted in Figure 16, the microneedles decreased in length with higher print speeds and constant print pressure. Conversely, increased length and thickness are observed with higher print pressures and constant print speed. Additional observations; regardless of print pressure, microneedles printed at the highest print speed (1000 mm/min) are consistently conical compared to the lower speeds (300mm/min and 600mm/min). However, the microneedles at lower print speeds became longer and more cylindrical as pressure increased.

3.1.5 Effect of Printing Liquid (Soy PC) Composition

The relationships between pressure, speed, the viscosity of print material, and gel-like properties of the support bath have been shown to have a great influence on the physical characteristics of microneedles. We identified from previous prints that increasing pressure at a constant speed will result in longer and thicker needles; due to the directly proportional relationship between flow rate and print pressure. There is also an inversely proportional relationship between print speed and flow rate. Lower print speeds result in more print material being extruded per unit of time, with constant print pressure.

The results thus far have shown that the support bath and print material rheological properties dictate how they interact. To further examine this interaction, additional prints are made with each soy PC composition supported by the 5 wt.% NPs bath.

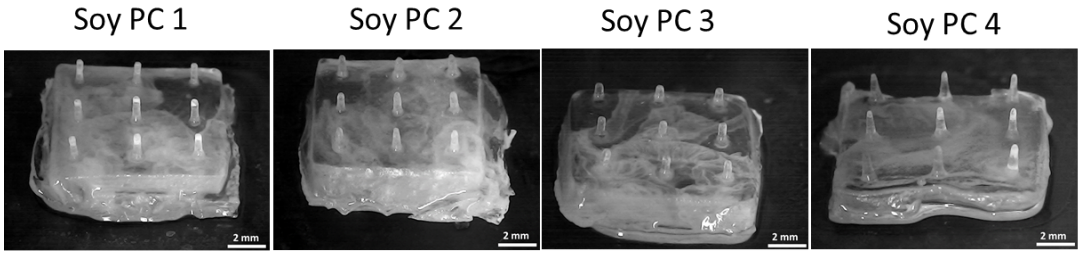

Figure 17: Soy PC 1-4 microneedle arrays printed in a castor oil bath containing 5 wt.% NPs using 30 G nozzle. Print speed of 1000 mm/min and print pressure of 70 kPa are used for all prints.

As shown in Figure 17, each soy PC composition resulted in microneedles with dissimilar physical characteristics, even though print pressure, print speed, and support

bath concentrations remained fixed. This is primarily due to the difference in flow behavior and viscosity of soy PC compositions when force is applied. Microneedles made with soy PC 4 had the most conical shape. Similar results could likely be achieved with soy PC 1-3 if different speed and print pressure combinations are used. However, more detailed experiments need to be conducted to make definite conclusions about this claim.

3.2 3D Printing Complications

Print analysis data indicate successful liquid-in-liquid 3D printing is dependent on the optimization of several factors. These factors include print speed, print pressure, nozzle size, printing material viscosity, and support bath gel behavior. An improper combination of these factors will result in prints with poor shape fidelity and resolution. Figure 18 below is an example of under-extrusion that stems from low print pressure. Low print pressure can cause insufficient extrusion resulting in discontinuities in printed microneedles [40]. Conversely, increasing the print pressure to an adequate level or using a larger diameter nozzle can increase the flow resulting in higher-resolution prints.

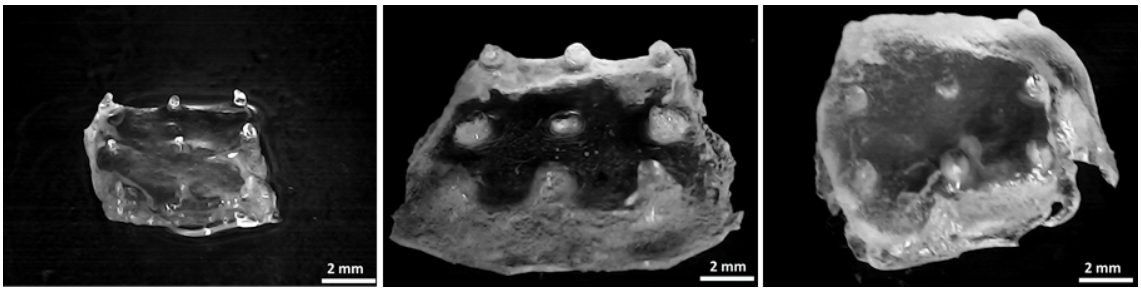

Figure 18: Examples of under-extrusion in microneedle structures due to low print pressure.

On the other hand, excessively high print pressures can have adverse effects, resulting in over-extrusion and unsteady flow. Over extrusion can be problematic when there are size constraints, as there are with microneedles. Often extrusion results in larger prints, exceeding the size constraint. Figure 19 shows how over-extrusion can affect the characteristics of microneedles.

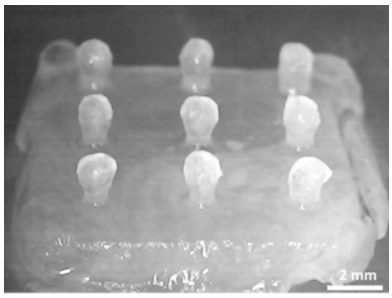

Figure 19: Examples of over-extrusion in microneedle structures due to excessively high print pressure.

The resulting microneedle size and shape are not conducive to skin penetration. In addition, over-extrusion affected the shape and size, resulting in microneedles with bulb-like shapes instead of conical or cylindrical. Microneedles with this shape will not be functional because of the tip radius. Decreasing the print pressure to adequate levels or using a smaller diameter nozzle can eliminate the over-extrusion problem.

Another by-product of excessively high pressure is unstable flows. This instability can lead to the deposition of print material in unintended places. Often this leads to an additional post-processing step that would otherwise be avoided if the flow is controlled. For example, Figure 20 shows the result of unstable flow (A) and the results after post-processing (B).

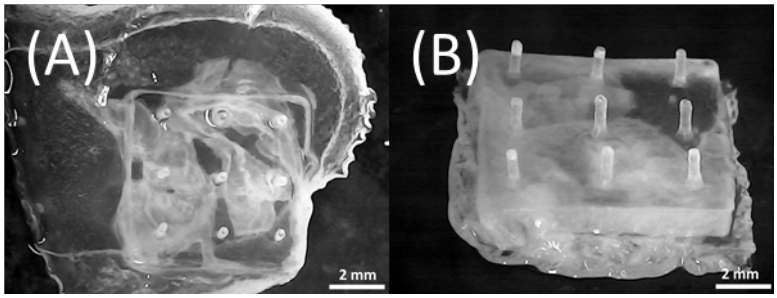

Figure 20: Unstable flow leads to unintended deposition of print material. (A) Extra material surrounding microneedle. (B) Post-processing was carried out to remove additional material.

Over-extrusion and unstable flow can add an extra step to the printing process. Therefore, microneedle print pressures must be tuned for continuous, stable, and uniform extrusion [40]. Clogged nozzles are also another source of printing complications. Clogged nozzles can lead to incomplete or faulty prints depending on the severity. Figure 21 shows examples of a clogged nozzle on the 3D printed structure.

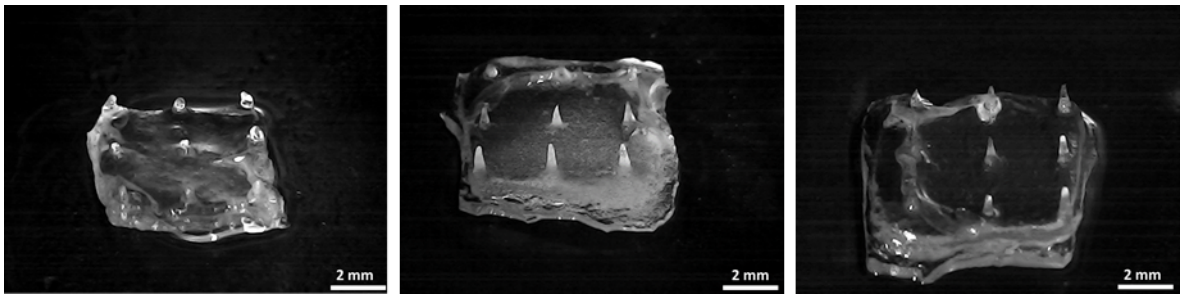

Figure 21: Results showing the effect of clogged nozzle 3D printed microneedle.

The inconsistency in microneedles due to the clogged nozzle can be resolved by gradually increasing the print pressure until there is a constant flow of print material or by manually using a pipette to remove the build of print material. Contaminants and viscosity

of print material can contribute to clogging of the nozzle. To minimize the number of complications during and after printing, it is important to optimize print parameters and viscosity of print materials and check the nozzle for adequate flow before printing.

3.3 Discussion and Conclusion

In this chapter, we investigated how liquid-in-liquid 3D printing can be used to make microneedles. We explored the effects of different print parameters on printed microneedle structures. We observed how changing print pressure, print speed, and nozzle size can ultimately affect the needle length, thickness, and shape. The results indicate a proportional relationship between flow rate and applied pressure; increased pressure resulted in increased flow rate, consistent with Equation 3.1 [41]. This resulted in longer needles when print pressure increases, provided the print speed is kept constant. Relative to flow rate, a lower print speed will result in a large volume of print material being extruded per unit time [41]. Results show that provided pressure is constant, microneedles printed at a lower speed are longer than those printed at a higher speed. It is essential to conclude that each printing material viscosity and possibly surface activity could determine how they responded to the print parameter. Also, the gel-like properties of the suspension bath can affect the resulting microneedles.

CHAPTER 4

MICRONEEDLE CHARACTERIZATION

4.1 Mechanical Properties of Microneedle

Compression tests are conducted on microneedle arrays consisting of nine (9) microneedles using a rheometer, as shown in Figure 8. A total of eight (8) tests are completed for two trials for each soy PC composition. Post-analysis is done on the force against displacement plots to find the fracture force for each soy PC composition. Figure 22 shows the force (in unit N) versus displacement (in unit μm) graph from the microneedle compression test for soy PC 1-4.

The resulting fracture force, indicated by the arrows, is the microneedle compressive strength or the load tolerable before failure. The fracture force is the stress corresponding to the first recorded failure for each microneedle array. The sudden drop in force indicates microneedle failure, the maximum force before this decrease in force is taken as a fracture force for each trial. Table 2 shows the resulting fracture forces from Figure 22.

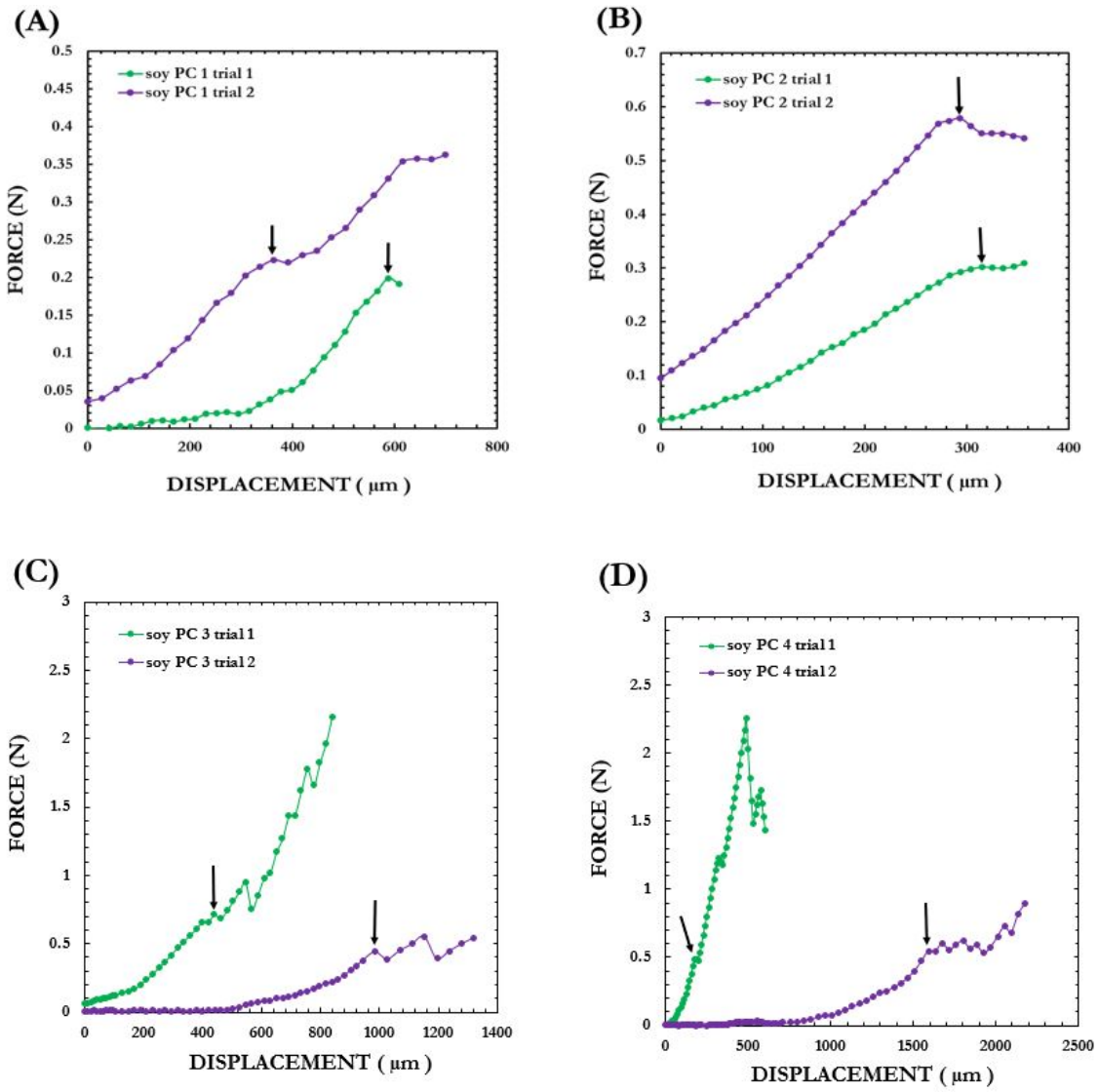

Figure 22: Force versus displacement graph from microneedle compression test showing the fracture force for soy PC 1-4 compositions.

The resulting fracture force values range between 0.199 N and 0.712 N, where soy PC 1, trial 1, has the lowest fracture force and soy PC 3, trial 1, has the highest fracture force. Of all the compositions, soy PC 1 has the lowest fracture force and standard

deviation. Soy PC 4 has the second-highest fracture force and second-lowest standard deviation. While the standard deviation for soy PCs 1 and 4 falls in acceptable ranges, it is too large for soy PCs 2 and 3, indicating the need for more sample measurements. Nevertheless, each test had a fracture force exceeding 0.058 N; the value reportedly needed to penetrate the stratum corneum (10 to 20 μm thick) [5, 42, 43]. This indicates that soy PC microneedles can potentially achieve penetration [42, 44–46].

Table 2: Results from Fracture forces from compression test.

Composition		Fracture Force
soy PC 1	trial 1	0.199
	trial 2	0.2333
	average	0.211
	std dev	$\pm$0.017
soy PC 2	trial 1	0.302
	trial 2	0.578
	average	0.440
	std dev	$\pm$0.195
soy PC 3	trial 1	0.712
	trial 2	0.442
	average	0.577
	std dev	$\pm$0.191
soy PC 4	trial 1	0.489
	trial 2	0.546
	average	0.517
	std dev	$\pm$0.040

The variability in fracture force between trials can be attributed to variations among individual microneedles in the array and/or variations between arrays used in each trial. For instance, Figure 23 consist of three microneedle arrays printed using the same

print material, print parameters, and suspension baths. Although similar, each microneedle possesses variations across the array and from sample to sample. These variations could lead to significant deviations in fraction forces when performing compression tests. In addition to microneedle variation, environmental conditions such as room temperature and humidity can affect test samples. Microneedles dehydrate once removed from ethanol. Since the test environment is not controlled during testing, there is a possibility each trial was exposed to different temperatures and humidity, affecting the rate of dehydration and shrinkage; potentially affecting performance. These test results are from a relatively small sample size; additional samples at controlled experimental conditions must be tested to provide better insight.

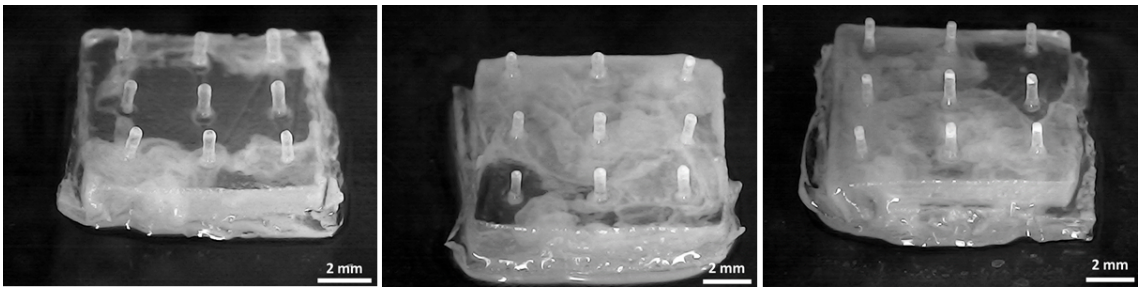

Figure 23: Variations in microneedles printed using the same print material, print parameters, and suspension bath.

4.2 Mechanical Properties of Printed Materials

Compression tests are conducted on square samples of each soy PC composition to understand the mechanical properties of the print materials and determine the stress-strain curves. One compression test was performed for each sample. Square samples of 0.015 m $\times$ 0.015 are printed and are used for this test, as shown in Figure 24. The area

of samples was calculated manually as $\approx 2.25 \times 10^{-3}$ m^2. All square samples are printed in castor oil baths containing 6 wt.% NPs using a 27G nozzle. The printed samples are illuminated by UV light for 5 minutes after being printed before removal from the support bath and 5 minutes after removal.

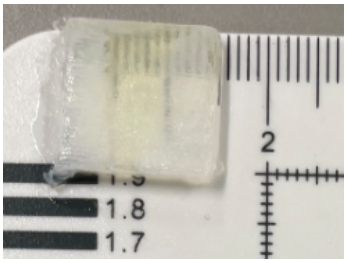

Figure 24: Square samples used for material characterization.

Figure 25 displays the resulting stress-strain curve obtained from the force-displacement data. The strain is the displacement divided by the initial distance between the top and bottom plates. The stress data is obtained by dividing the recorded force by the area of the samples; the area was measured by areas of printed samples. Here, the compressive modulus is the parameter of interest as it is an intrinsic property that quantifies the stiffness of each soy PC structure when a uni-axial compressive force is applied.

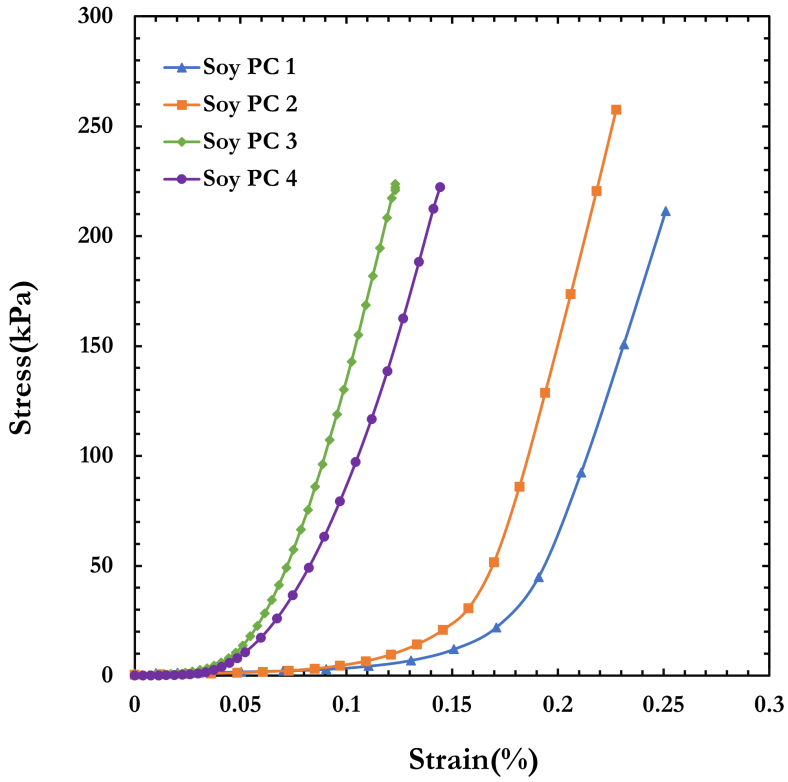

Figure 25: Stress versus strain graph from compression test of printed materials (square shape) made from soy PCs 1-4.

Figure 26 shows the initial sections of the stress-strain curves with the equation for fitted trend lines. The compressive modulus is the slope of the curve. This property is important because it affects the mechanical strength of the microneedle. Different compositions of soy PC are prepared to optimize for print material with a high compressive modulus, good printability, and appropriate response to photopolymerization.

The mechanical properties of each soy PC responded to the tuning of each constituent component, as shown in Figure 25 and Figure 26. The compressive modulus of

soy PC 1, soy PC 2, soy PC 3, and soy PC 4 is found to be 13.58, 17.42, 26.05, and 10.53 kPa, respectively. Based on the results, the soy PC 3 (with the highest PEGDA content compared to soy PCs 1 and 2, while having the highest lipid content, as described in Table 1) has the highest compressive modulus. That could be due to the strongest lipid-castor oil surface activity (of soy PC 3 that stems from the highest lipid content) resulting [23].

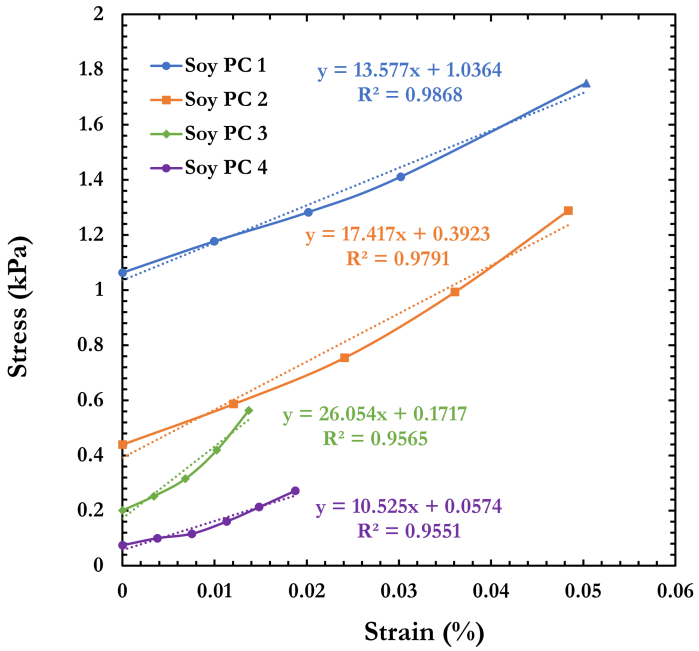

Figure 26: The onset of stress versus strain graph from compression test (Figure 25 of square soy PC 1-4 samples accompanied by the fitted trend lines and their equations.

Further investigation is needed to determine the critical factors affecting the compressive modulus. The expectation is increasing the $Vol\%$ of PEGDA will increase material stiffness. This was observed when the volume percentage was increased from 36

$Vol\%$ to 54 $Vol\%$ (from soy PC 1 to soy PC 3). However, a decrease in compressive modulus was observed from 54 $Vol\%$ to 85 $Vol\%$. It is important to note that the soy PC $Vol\%$ decreased going from soy PC 3 to soy PC 4; this result could be attributed to the ratios of the constituents and potentially the importance of the surface activity of lipids on the compressive modulus. This is because of the fact that higher soy PC can contribute to a higher association degree with castor oil, leading to better mechanical performance on the final product [23]. These test results are from a relatively small sample size, so the microneedle mechanical properties should be treated as preliminary results and analyzed with caution. Additional samples need to be tested to provide a more accurate conclusion.

4.3 Microneedle Penetration Test

To achieve effective drug delivery, microneedles must be able to pierce the outermost layer of the epidermis (10 to 20 μm) without breaking or bending during penetration [5]. The microneedle ability to effectively penetrate the skin is dependent on several factors. These include material properties, microneedle geometry, microneedle length, tip-radius, and base diameter [36]. Besides microneedle characteristics, skin elasticity and thickness will also affect penetration performance. Optimal design is important because rupturing of microneedles during or after application may affect the drug release profile, which could result in premature drug release [5].

To investigate the effectiveness of the 3D-printed microneedles, a commercial polymeric film is evaluated as a model membrane for microneedle (MN) insertion. Parafilm was shown to be a suitable skin simulant in previous studies [5, 36].

A total of four trials are completed using soy PC 1-4 Microneedle arrays. Each sample is tested on a single sheet of Parafilm, approximately 127μm in thickness. Successful penetration is only achieved using the soy PC 4 microneedle. Figure 27 shows the results from penetrating the single layer of Parafilm. The microneedle array in Figure 27 is printed in a castor oil bath containing 5 wt.% nanoparticles, using a print pressure of 70 kPa and a print speed of 1000 mm/min.

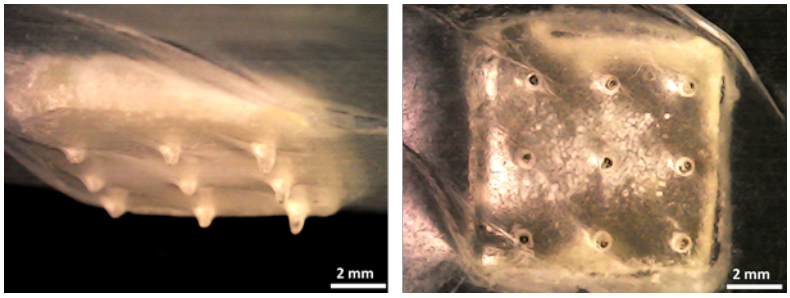

Figure 27: Penetration test performed on a single layer of Parafilm.

Since the soy PC 4 microneedle array is successful in the single-layer penetration, an additional test is performed using two layers of Parafilm. Figure 28 shows an unsuccessful attempt to pierce two layers of Parafilm approximately 254 μm in thickness. Prior studies used eight (8) layers of folded Parafilm (approximately 1 mm thick) to mimic neonatal porcine skin, which is often used as a model of the human skin because the structural similarities [36, 47].

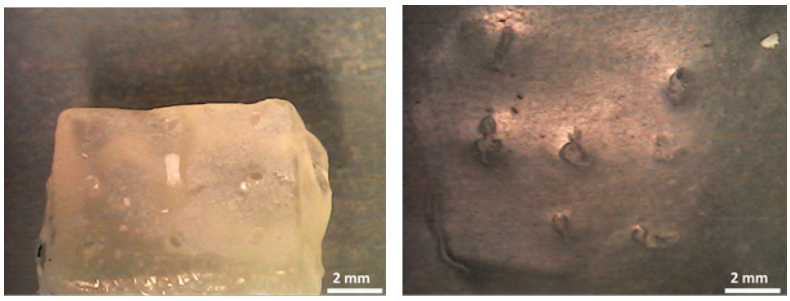

Figure 28: Penetration test performed on a double layer of Parafilm.

Composition	Number of Parafilm Layers (1 or 2)	Success (Yes/No)
soy PC 1	1	No
soy PC 2	1	No
soy PC 3	1	No
soy PC 4	1	Yes
	2	No

Table 3: Results of Penetration Test

The soy PC 4 microneedles that successfully penetrated the single layer of Parafilm (127μm in thickness) possessed a more conical geometry when compared to soy PC 1-3 microneedles, as evident in Figure 17. The failure to penetrate Parafilm using soy PC 1-3 could be attributed to the difference in geometry, as depicted in Figure 17. Even though soy PC 3 had the highest fracture force and compressive modulus, the geometry may have limited penetration. Numerous studies have indicated that geometries with larger tip radii can decrease the probability of successful penetration due to wider contact angle [5, 48]. The microneedles produced using the embedded 3D printing process are primarily cylindrical or conical, as shown in Figure 29.

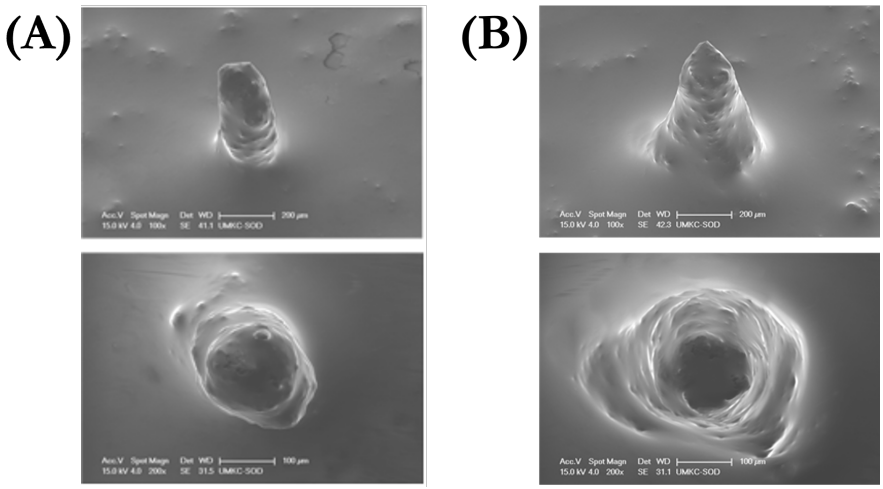

Figure 29: Scanning electron images of the microneedle. (A) Tilted and top view of a single cylindrical microneedle and (B) tilted and top view of a single conical shape microneedle.

4.4 Discussion and Conclusion

Mechanical characterization is an essential part of the manufacturing process of Microneedles. The printed samples are characterized using compression tests because they imitate the nature of forces that will be present during skin penetration. The key takeaways from the compression test are the mechanical fracture force and compressive modulus for each soy PC composition. Both of these factors provided valuable insight into the design and material properties of the microneedles. The mechanical and material characterization results indicate that soy PC 3 has the highest fracture force and compressive moduli. These results can be used to optimize microneedles performance and inform design decisions.

A commercial polymeric film is utilized as a skin resemblance for the penetration

test [5,36,49]. Starting with one layer of Parafilm (127μm in thickness), microneedles are manually administered to test for penetration. Soy PC 1-4 are evaluated for penetration of one (1) layer of polymer; however, successful penetration is only achieved using soy PC 4. Even though Soy PC 3 has the highest fracture force and compressive modulus, the microneedles cannot penetrate the Parafilm. Mechanical properties are important for penetration, however, penetration also depends on other factors, such as geometry. The geometry of the soy PC 3 microneedles may have been the limiting factor, preventing successful penetration. These are preliminary tests; the results indicate that microneedle geometry and mechanical properties must be optimized for skin penetration. Even though the results show the printed microneedles were not well suited for skin penetration, they could be suitable for mucosal tissues (such as nasal and oral cavities) that often have a single-cell thick epidermis.

CHAPTER 5

CONCLUSION AND FUTURE WORK

5.1 Conclusion

This study presents a preliminary framework for creating microneedles using a liquid-in-liquid 3D printing approach (embedded 3D printing) coupled with an associative surfactant system. We could print microneedles using a new class of materials (lipid-hydrogel) that are sustainable and comprise natural cell membranes and tissues.

Previous studies indicated that this process could fabricate relatively complex structures. However, creating micro-scale structures to function as a drug delivery device added another level of complexity. The first task was to understand how the print parameters and materials determined the resulting characteristics of printed microneedles. These factors included print speed, print pressure, nozzle size, print material viscosity, and support bath gel properties. Data from previous studies were referenced to minimize the parameter space. With this insight, the value of each parameter was systematically changed to observe the effects on the resulting microneedles and underlying relationships.

There is a directly proportional relationship between flow rate and print pressure and flow rate and nozzle size. Microneedles were longer and thicker when print pressure was increased, provided the print speed was kept constant. Larger nozzle sizes resulted in thicker microneedles with constant print pressure and speed. The effects of the print speed were relative to the flow rate. Higher print speeds resulted in a smaller volume of print

material being extruded over time, and low print speeds resulted in the opposite [41, 50]. The relationship of the print material to print parameters was dependent on the soy PC viscosity. Each Soy PC composition responded differently when subjected to the same print parameters and deposited in the same support bath.

Throughout this research, multiple iterations of microneedles were printed using four print materials, two support baths, and the print parameters previously listed. Numerous microneedles were printed to optimize for ideal mechanical properties and extensive physical properties suited for skin penetration. The results confirmed printing technique was capable of printing microneedles with good shape fidelity and tunable extensive physical properties (i.e., shape, length, and thickness). Being able to tune the physical properties is crucial for creating microneedles for various applications.

Compression tests were conducted to understand the mechanical properties better and simulate the assumed application force. Compression testing highlighted details about the mechanical fracture force of printed microneedles and the compressive modulus of each printed material. These properties, in tandem with the results from the penetration test conducted using Parafilm wax paper, provided insight into the resulting ability of microneedles to penetrate the skin effectively. Even though progress has been made in fabricating the microneedles, optimizing for penetration has proven to be a challenge throughout this research. In conclusion, results show our microneedles were not well suited for skin penetration; however, they could be suitable for mucosal tissues (such as nasal and oral cavities) drug delivery that often have a single-cell thick epidermis.

5.2 Future Directions

3D printing microneedles via an embedded 3D printing process for an associative system is a promising technique. This approach to microneedle manufacturing can create opportunities for numerous innovations. Future work will be conducted to understand better key factors such as print material and support bath rheology, print material/suspension bath interaction, and print material flow characteristics. Rheological characterization of the print materials and suspension baths will provide the ability to quantify behaviors associated with different properties, such as viscosity. In addition to investigating rheology, design changes will be implemented to print substrates and microneedles with different print materials. Even though the PA as a macromolecule drug model was added for two printing materials, their investigation will be included in future work. Subsequently, allowing for more efficient drug loading as drugs can be isolated to only the microneedles instead of the microneedles and substrate. After drug loading, the effectiveness of macromolecular drug delivery and release will be investigated.

Skin penetration is important for effective drug delivery and will be addressed in plans. Microneedle spacing, density (number of microneedles in an array), geometry, tip-radius, and mechanical properties are important factors that aid penetration. Spacing and density can be addressed fairly quickly through G-code design change. Once implemented, penetration can be analyzed as a microneedle spacing and density function. Penetration can also be analyzed as a function of the geometry, height, and fracture force of microneedles and material properties. Future works will include more detailed characterization and measurements, including compression testing according to standardized

testing such as ASTM.

REFERENCE LIST

[1] Y.-C. Kim, J.-H. Park, and M. R. Prausnitz, "Microneedles for drug and vaccine delivery," *Advanced Drug Delivery Reviews*, vol. 64, no. 14, pp. 1547–1568, 2012.

[2] "CELLINK BIO X6 BIOPRINTER," https://www.cellink.com/bioprinting/bio-x6-3d-bioprinter/, note = Accessed: 01-02-2023.

[3] "AMSCOPE DIGITAL MICROSCOPE," https://amscope.com/collections/digital-microscopes-kids-handheld-microscope, note = Accessed: 01-02-2023.

[4] "TA INSTRUMENT DISCOVERY HYBRID RHEOMETER," https://www.tainstruments.com/hr-10/, note = Accessed: 01-02-2023.

[5] P. Makvandi, M. Kirkby, A. R. Hutton, M. Shabani, C. K. Yiu, Z. Baghbantaraghdari, R. Jamaledin, M. Carlotti, B. Mazzolai, V. Mattoli *et al.*, "Engineering microneedle patches for improved penetration: analysis, skin models and factors affecting needle insertion," *Nano-Micro Letters*, vol. 13, no. 1, pp. 1–41, 2021.

[6] M. S. Chellathurai, V. W. Ling, and V. Palanirajan, "Fabrication and evaluation of transdermal microneedles for a recombinant human keratinocyte growth factor," *Turkish Journal of Pharmaceutical Sciences*, vol. 18, no. 1, p. 96, 2021.

[7] J. S. Kochhar, W. J. Soon, J. Choi, S. Zou, L. Kang *et al.*, "Effect of microneedle geometry and supporting substrate on microneedle array penetration into skin," *Journal of Pharmaceutical Sciences*, vol. 102, no. 11, pp. 4100–4108, 2013.

[8] Y. N. Kalia, V. Merino, and R. H. Guy, "Transdermal drug delivery: clinical aspects," *Dermatologic Clinics*, vol. 16, no. 2, pp. 289–299, 1998.

[9] A. Ahad, M. Aqil, K. Kohli, H. Chaudhary, Y. Sultana, M. Mujeeb, and S. Talegaonkar, "Chemical penetration enhancers: a patent review," *Expert Opinion on Therapeutic Patents*, vol. 19, no. 7, pp. 969–988, 2009.

[10] M. Goldberg and I. Gomez-Orellana, "Challenges for the oral delivery of macromolecules," *Nature Reviews Drug Discovery*, vol. 2, no. 4, pp. 289–295, 2003.

[11] M. R. Prausnitz and R. Langer, "Transdermal drug delivery," *Nature Biotechnology*, vol. 26, no. 11, pp. 1261–1268, 2008.

[12] D. P. Wermeling, S. L. Banks, D. A. Hudson, H. S. Gill, J. Gupta, M. R. Prausnitz, and A. L. Stinchcomb, "Microneedles permit transdermal delivery of a skin-impermeant medication to humans," *Proceedings of the National Academy of Sciences*, vol. 105, no. 6, pp. 2058–2063, 2008.

[13] S. P. Davis, B. J. Landis, Z. H. Adams, M. G. Allen, and M. R. Prausnitz, "Insertion of microneedles into skin: measurement and prediction of insertion force and needle fracture force," *Journal of Biomechanics*, vol. 37, no. 8, pp. 1155–1163, 2004.

[14] M. A. Luzuriaga, D. R. Berry, J. C. Reagan, R. A. Smaldone, and J. J. Gassensmith, "Biodegradable 3d printed polymer microneedles for transdermal drug delivery," *Lab on a Chip*, vol. 18, no. 8, pp. 1223–1230, 2018.

[15] W. K. Raja, S. MacCorkle, I. M. Diwan, A. Abdurrob, J. Lu, F. G. Omenetto, and D. L. Kaplan, "Transdermal delivery devices: fabrication, mechanics and drug release from silk," *Small*, vol. 9, no. 21, pp. 3704–3713, 2013.

[16] S. Xie, Z. Li, and Z. Yu, "Microneedles for transdermal delivery of insulin," *Journal of Drug Delivery Science and Technology*, vol. 28, pp. 11–17, 2015.

[17] S. N. Economidou, C. P. Pissinato Pere, M. Okereke, and D. Douroumis, "Optimisation of design and manufacturing parameters of 3d printed solid microneedles for improved strength, sharpness, and drug delivery," *Micromachines*, vol. 12, no. 2, p. 117, 2021.

[18] F. Meng, A. Hasan, M. M. N. Babadaei, P. H. Kani, A. J. Talaei, M. Sharifi, T. Cai, M. Falahati, and Y. Cai, "Polymeric-based microneedle arrays as potential platforms in the development of drugs delivery systems," *Journal of Advanced Research*, vol. 26, pp. 137–147, 2020.

[19] P. Janphuang, M. Laebua, C. Sriphung, P. Taweewat, A. Sirichalarmkul, K. Sukjantha, N. Promsawat, P. Leuasoongnoen, S. Suphachiaraphan, K. Phimol *et al.*, "Polymer based microneedle patch fabricated using microinjection moulding," in *MATEC Web of Conferences*, vol. 192. EDP Sciences, 2018, p. 01039.

[20] H. Zhang, H. Liu, and N. Zhang, "A review of microinjection moulding of polymeric micro devices," *Micromachines*, vol. 13, no. 9, p. 1530, 2022.

[21] S. Choo, S. Jin, and J. Jung, "Fabricating high-resolution and high-dimensional microneedle mold through the resolution improvement of stereolithography 3d printing," *Pharmaceutics*, vol. 14, no. 4, p. 766, 2022.

[22] S. Mckee, A. Lutey, C. Sciancalepore, F. Poli, S. Selleri, and A. Cucinotta, "Microfabrication of polymer microneedle arrays using two-photon polymerization," *Journal of Photochemistry and Photobiology B: Biology*, vol. 229, p. 112424, 2022.

[23] H. Honaryar, J. A. LaNasa, E. C. Lloyd, R. J. Hickey, and Z. Niroobakhsh, "Fabricating robust constructs with internal phase nanostructures via liquid-in-liquid 3d printing," *Macromolecular Rapid Communications*, vol. 42, no. 22, p. 2100445, 2021.

[24] A. McCormack, C. B. Highley, N. R. Leslie, and F. P. Melchels, "3d printing in suspension baths: keeping the promises of bioprinting afloat," *Trends in Biotechnology*, vol. 38, no. 6, pp. 584–593, 2020.

[25] S. Chen, W. S. Tan, M. A. Bin Juhari, Q. Shi, X. S. Cheng, W. L. Chan, and J. Song, "Freeform 3d printing of soft matters: recent advances in technology for biomedical engineering," *Biomedical Engineering Letter*, vol. 10, no. 4, pp. 453–479, 2020.

[26] H. Honaryar, S. Amirfattahi, and Z. Niroobakhsh, "Associative liquid-in-liquid 3d printing techniques for freeform fabrication of soft matter," *Small*, 2023, https://doi.org/10.1002/smll.202206524.

[27] S. Shi and T. P. Russell, "Nanoparticle assembly at liquid–liquid interfaces: From the nanoscale to mesoscale," *Advanced Materials*, vol. 30, no. 44, p. 1800714, 2018.

[28] H. Honaryar, J. A. LaNasa, R. J. Hickey, J. C. Shillcock, and Z. Niroobakhsh, "Investigating the morphological transitions in an associative surfactant ternary system," *Soft Matter*, vol. 18, no. 13, pp. 2611–2633, 2022.

[29] C. Loebel, C. B. Rodell, M. H. Chen, and J. A. Burdick, "Shear-thinning and self-healing hydrogels as injectable therapeutics and for 3d-printing," *Nature Protocols*, vol. 12, no. 8, pp. 1521–1541, 2017.

[30] H. Honaryar, *Interfacial Self-Assemblies of Surfactants at Water-Oil Interfaces*. University of Missouri-Kansas City, 2021.

[31] Z. Niroobakhsh, J. A. LaNasa, A. Belmonte, and R. J. Hickey, "Rapid stabilization of immiscible fluids using nanostructured interfaces via surfactant association," *Physical Review Letters*, vol. 122, no. 17, p. 178003, 2019.

[32] Z. Niroobakhsh, *Viscoelastic Surfactant/Fatty Acid Interfaces: Fluid Dynamics, Rheology, and Structure*. The Pennsylvania State University, 2017.

[33] Z. Niroobakhsh and A. Belmonte, "Dynamics of a reactive micellar oil-water interface in a flowing liquid column," *Journal of Non-Newtonian Fluid Mechanics*, vol. 261, pp. 111–122, 2018.

[34] F. Ercole, M. R. Whittaker, J. F. Quinn, and T. P. Davis, "Cholesterol modified self-assemblies and their application to nanomedicine," *Biomacromolecules*, vol. 16, no. 7, pp. 1886–1914, 2015.

[35] R. M. Capito, H. S. Azevedo, Y. S. Velichko, A. Mata, and S. I. Stupp, "Self-assembly of large and small molecules into hierarchically ordered sacs and membranes," *Science*, vol. 319, no. 5871, pp. 1812–1816, 2008.

[36] E. Larrañeta, J. Moore, E. M. Vicente-Pérez, P. González-Vázquez, R. Lutton, A. D. Woolfson, and R. F. Donnelly, "A proposed model membrane and test method for microneedle insertion studies," *International Journal of Pharmaceutics*, vol. 472, no. 1-2, pp. 65–73, 2014.

[37] S. P. Sutera and R. Skalak, "The history of poiseuille's law," *Annual review of fluid mechanics*, vol. 25, no. 1, pp. 1–20, 1993.

[38] I. Szabó, *Geschichte der mechanischen Prinzipien: und ihrer wichtigsten Anwendungen*. Springer-Verlag, 2013, vol. 32.

[39] G. G. Stokes, "On the theories of the internal friction of fluids in motion, and of the equilibrium and motion of elastic solids," *Transactions of the Cambridge Philosophical Society*, vol. 8, 1880.

[40] S. Ramesh, O. L. Harrysson, P. K. Rao, A. Tamayol, D. R. Cormier, Y. Zhang, and I. V. Rivero, "Extrusion bioprinting: Recent progress, challenges, and future opportunities," *Bioprinting*, vol. 21, p. e00116, 2021.

[41] E. N. Udofia and W. Zhou, "Microextrusion based 3d printing–a review," in *2018 International Solid Freeform Fabrication Symposium*. University of Texas at Austin, 2018.

[42] R. S. Bhadale and V. Y. Londhe, "A systematic review of carbohydrate-based microneedles: Current status and future prospects," *Journal of Materials Science: Materials in Medicine*, vol. 32, no. 8, pp. 1–17, 2021.

[43] M. Ali, S. Namjoshi, H. A. Benson, Y. Mohammed, and T. Kumeria, "Dissolvable polymer microneedles for drug delivery and diagnostics," *Journal of Controlled Release*, vol. 347, pp. 561–589, 2022.

[44] K. J. Cha, T. Kim, S. J. Park, and D. S. Kim, "Simple and cost-effective fabrication of solid biodegradable polymer microneedle arrays with adjustable aspect ratio for transdermal drug delivery using acupuncture microneedles," *Journal of Micromechanics and Microengineering*, vol. 24, no. 11, p. 115015, 2014.

[45] J. D. Kim, M. Kim, H. Yang, K. Lee, and H. Jung, "Droplet-born air blowing: Novel dissolving microneedle fabrication," *Journal of Controlled Release*, vol. 170, no. 3, pp. 430–436, 2013.

[46] J.-H. Park, M. G. Allen, and M. R. Prausnitz, "Biodegradable polymer microneedles: fabrication, mechanics and transdermal drug delivery," *Journal of controlled release*, vol. 104, no. 1, pp. 51–66, 2005.

[47] B. Pamornpathomkul, T. Ngawhirunpat, I. A. Tekko, L. Vora, H. O. McCarthy, and R. F. Donnelly, "Dissolving polymeric microneedle arrays for enhanced site-specific acyclovir delivery," *European Journal of Pharmaceutical Sciences*, vol. 121, pp. 200–209, 2018.

[48] S. Aoyagi, H. Izumi, and M. Fukuda, "Biodegradable polymer needle with various tip angles and consideration on insertion mechanism of mosquito's proboscis," *Sensors and Actuators A: Physical*, vol. 143, no. 1, pp. 20–28, 2008.

[49] M. Kirkby, A. B. Sabri, D. Scurr, and G. Moss, "Microneedle-mediated permeation enhancement of chlorhexidine digluconate: Mechanistic insights through imaging mass spectrometry," *Pharmaceutical Research*, pp. 1–14, 2022.

[50] C.-P. Chen, H.-X. Li, and H. Ding, "Modeling and control of time-pressure dispensing for semiconductor manufacturing," *International Journal of Automation and Computing*, vol. 4, no. 4, pp. 422–427, 2007.

VITA

Romario Dyke was born November 28, 1994, in Kingston, Jamaica. He attended Wolmers Boys High school. After graduating high school, he started his bachelor's studies at the University of Mount Olive pursuing a degree in Chemistry. While attending, he played on his college soccer team. Romario later transferred to the University of Missouri-Kansas City, where he completed his Bachelor's in Mechanical Engineering with a major in Chemistry. Through his years at the University of Missouri-Kansas City, Romario was a member of the National Society of Black Engineers and a student manager at the Student Union. Romario joined Dr. Niroobakhsh's research group as a graduate research student in the Fall of 2021. Upon his graduation, he will continue his career aspirations in the Mechanical Engineering research field.